Contrib Mineral Petrol (2007) 153:289–301
DOI 10.1007/s00410-006-0147-7

ORIGINAL PAPER

Intersector element partitioning in tourmaline: a potentially powerful single crystal thermometer

Vincent J. van Hinsberg · John C. Schumacher

Received: 3 May 2006 / Accepted: 12 September 2006 / Published online: 3 November 2006

Abstract Hourglass sector zoning, and related polar overgrowths, are common features of metamorphic tourmaline, developing as a result of variations in element preference on the different growth surfaces. For sector-zoned crystals, three domains are present for each growth zone (c^+, c^- and a), with compositional differences most distinct for Ca and Ti, and among c^+ and c^- sectors. Intersector differences vary, commonly showing decreasing fractionation from core to rim attributed to increasing metamorphic grade. Here we show that intersector element partitioning is temperature dependent and derive empirical geothermometers based on c^+–$c^-$and c^+–a partitioning of Ca and Ti. These thermometers are applicable over a range of temperatures and bulk-rock compositions. Intersector partitioning is not affected by re-equilibration and records and preserves complete T-histories of individual tourmaline grains from prograde to peak and on to retrograde growth. Information on element mobility is preserved by tourmaline composition, because intersector partitioning is independent of element concentration. These factors make intersector partitioning an ideal tool to elucidate the thermal history of tourmaline grains and thus their host environment and tourmaline's refractory nature preserves these signatures even into the sedimentary record.

Keywords Intersector · Geothermometer · Tourmaline · Sector zoning · Thermal history

Communicated by J. Hoefs.

Electronic supplementary material Supplementary material is available in the online version of this article at http://dx.doi.org/10.1007/s00410-006-0147-7 and is accessible for authorized users.

V. J. van Hinsberg (✉) · J. C. Schumacher
Department of Earth Sciences, University of Bristol,
Wills Memorial Building, Queen's Road,
Bristol BS8 1RJ, UK
e-mail: V.J.vanHinsberg@gmx.net

Introduction

Geothermobarometry

Geothermobarometers are one of the key tools of metamorphic and igneous petrologists to unravel the P–T conditions and evolution of rocks and melts. The most widely applied of these is the garnet–biotite exchange thermometer, based on a systematic change in Mg–Fe partitioning with temperature [(Holdaway 2000), and references therein]. A wide variety of thermobarometers is now available, using the majority of common rock-forming minerals, as well as a number of accessory phases [e.g. monazite (Pyle and Spear 2000), xenotime (Pyle et al. 2001), and rutile (Zack et al. 2004)]. Most of these thermometers are based on the exchange of elements between two co-existing phases, e.g. Mg–Fe exchange between garnet and biotite (Holdaway 2000), Ca–Na–K exchange between coexisting feldspars (Elkins and Grove 1990), and Fe–Mn exchange between garnet and ilmenite (Powneeby et al. 1991). Geobarometers are mainly net-transfer reactions involving more than two phases, such as the garnet–rutile–aluminosilicate–ilmenite–quartz barometer (GRAIL Bohlen et al. 1983), and the garnet–aluminosilicate–quartz–plagioclase barometer (GASP Holdaway 2001). Miscibility gaps and mineral solvi

provide further opportunities for thermobarometry (e.g. muscovite–paragonite solvus thermometry Blencoe et al. 1994). Intersite thermometry [e.g. distribution of Mg and Fe between the *M*-sites of pyroxene (Grover and Orville 1969)] is another powerful technique, but is analytically challenging, because the site distribution of elements is difficult to determine. Recently, focus has shifted towards the solubility of minor elements in a saturated environment to derive temperature estimates [e.g. the Ti in biotite thermometer (Henry et al. 2005) and the Zr in rutile thermometer (Zack et al. 2004)].

Despite the implied success of widespread use of geothermobarometers, problems of obtaining accurate temperatures and pressures still persist. These difficulties are mainly related to the identification of coexisting equilibrium compositions among the geothermobarometry phases. Preserving equilibrium compositions during cooling accompanying uplift and exhumation is a problem, given that the closure temperature for diffusion in minerals is generally (well) below that of peak metamorphism and differs strongly among minerals (e.g. garnet having a higher closure *T* than its biotite companion). Retrograde overprint reactions involving these phases can further complicate the choice of equilibrium compositions used for thermobarometry. Examples include the chloritisation of biotite, which results in the redistribution of Mg and Fe between these phases and albitisation of plagioclase rendering barometers using the anorthite component of plagioclase ineffective (e.g. GASP). For geothermobarometers involving more than two phases these problems are generally more pronounced.

Solubility thermometers [e.g. Ti in biotite (Henry et al. 2005), Zr in rutile (Zack et al. 2004)] are less influenced by these factors, which explains their current appeal. However, interpreting the temperatures derived from individual grains, and zones in grains, in terms of the *P*–*T* evolution of its host can be difficult (except for the maximum *T* attained). Where grains are present as inclusions and textures can hence facilitate such interpretations, it is generally not possible to conclusively demonstrate that the saturation criteria have been met, and exchange with the inclusion's host could have altered an element's concentration. Still, combined with careful petrography and assessment of any compositional zoning, these thermometers have great potential.

Tourmaline thermometry

Henry and Dutrow (1992, 1996) proposed a different type of thermometer, based on the difference between coeval overgrowths on the c^+ and c^- pole of tourmaline. They showed that the extent of the compositional difference correlates inversely with metamorphic grade, especially with temperature. Compositional differences between c^+ and c^- result from variations in dipolar surface charge and site morphology on the growth surfaces in the c^+ and c^- directions. These surface characteristics lead to a preference for more highly charged cations on the c^- side of the mineral, as well as a full *X*-site. Conversely, the c^+ side prefers lower charged cations and vacancies on the *X*-site (Henry and Dutrow 1992, 1996; van Hinsberg et al. 2006). The rationale for a temperature dependence on these interpolar compositional differences is that the capacity to fractionate elements will decrease as the temperature increases. For one, the polar surface charges will decrease as the vibrational energy of the site increases with increasing *T* and, secondly, the site morphology control will decrease as the bond lengths and angles become more flexible at high *T*. This is comparable to the observed decreasing fractionation of isotopes with increasing temperature (Faure 1986).

There is no direct exchange of elements between the polar overgrowths; instead, they ''communicate'' through the host medium. In an evolving metamorphic rock, fluids will be the dominant transport medium and hence control this exchange. Because this fluid is a continuous phase of identical composition at either pole, the exchange between the poles can be modelled as direct exchange in thermodynamic terms (i.e. the reaction pathway is unimportant). Use of the term ''distribution coefficient'' seems therefore warranted for this type of exchange and general models for element distribution between phases should be applicable to interpolar exchange. *D* values are dependent on *P*, *T* and composition of the exchanging phases. Similarly, interpolar distribution will be controlled by these variables. The exchanging tourmaline sectors will both adjust their composition in reaction to changes in their growth environment. On top of that, their sector-zoning-controlled element preference will change and hence the distribution coefficient between the sectors. Because sector-zoning effects are most pronounced in minor and trace elements, the bulk compositional variations between sectors are limited. Effects of phase composition on element distribution will therefore be minimal. Temperature dependence on the distribution coefficient has been observed, as described above. A pressure dependence has not been demonstrated, but is probably present. Incorporation of cations with an ionic radius different from the ideal site dimensions will have a volume effect associated with it, which should result in a pressure dependence for this incorporation.

However, it remains to be seen whether the variations in composition observed in sector zoning are sufficient to lead to a significant pressure contribution.

The differences between polar overgrowths are most pronounced for Ca and Ti, with interpolar variations commonly exceeding the growth zoning variations (e.g. Sperlich 1990). These elements, therefore, seem the most promising thermometers and an empirical formulation for a Ca/Na interpolar thermometer was presented by Henry and Dutrow (1996). Henry and Dutrow (1992, 1996), Sperlich (1990) and Sperlich et al. (1996) show that the temperature range recorded by this thermometer is on the order of 300–650°C, above which the compositional differences between polar overgrowths are indistinguishable. Moreover, this thermometer is independent of a saturating phase for either Ca or Ti, because it is based on the difference between parts of the crystal grown under the same conditions of *P, T* and activity of the chemical components. Consequently, it provides a powerful single crystal thermometer, applicable over a wide range of conditions, but especially useful for low-*T* conditions where few other thermometers are available. The widespread occurrence of tourmaline coupled with its resistance to alteration and weathering, further allows this thermometer to be applied to a wide variety of geological environments (e.g. the various chapters in Grew and Anovitz 1996). However, the uncertainty in the calibration of the tourmaline interpolar thermometer is still a concern (Henry and Dutrow 1996).

Tourmaline sector zoning as described by Henry et al. (1999) and van Hinsberg et al. (2006) is a different manifestation of the polar overgrowth phenomenon, in that the crystallographic mechanisms controlling the different sector compositions are identical to those operating for polar overgrowths. However, the number of different compositions for every growth zone is increased, because an intermediate sector along the *a*-axis will be present (Fig. 1). The $m(10\bar{1}0)$ and $a(11\bar{2}0)$ growth surfaces that are responsible for the formation of this ''*a*'' quadrant or sector are not influenced by polar charge or site morphology in the *c*-direction, as they are perpendicular to this orientation. Van Hinsberg et al. (2006) concluded that the *a*-sector composition was the equivalent tourmaline composition not affected by sector zoning. Furthermore, splitting of the *c*-sectors due to growth on additional crystallographic planes has been observed, originally in tourmalines from the island of Syros (Cyclades, Greece – van Hinsberg et al. 2006), but it has now also been observed in metapelitic tourmalines from the French Massif Central. This splitting is probably due to growth in the *c*-directions of both the $r(10\bar{1}1)$ and $o(02\bar{2}1)$ faces of tourmaline, and has also been observed by Henry et al. (1999). Because these faces have a different angle to the electric field set up by the dipolar charge along the *c*-axis and different surface site morphology, varying intensities of sector zoning are realised.

These sector differences are decidedly *not* a disequilibrium feature, but form as a result of different local equilibria between the various growth surfaces and their identical host environment. Systematic compositional, textural and optical properties for the different sectors in tourmalines from widely varying *P–T–X* hosts are incompatible with a disequilibrium control on their formation, as are the temperature dependence features described below. Sectors are, however, in disequilibrium away from the growth surface (in the crystal bulk), and it is only for the slow diffusion rates inferred for tourmaline (e.g. Voll 1969; von Goerne et al. 1999a) that they avoid diffusional elimination.

Because sector zoning forms by the same mechanism as polar overgrowths, temperature dependent partitioning of elements among sectors is implied. This *T* dependence has indeed been observed by van Hinsberg et al. (2004, 2006) and confirms that intersector differences can be used as a thermometer. Similar to the interpolar geothermometer, its intersector equivalent is a single-crystal thermometer, but it has some additional advantages. For every growth zone, at least five intersector apparent distribution coefficients (*D*) are present (apparent because no direct exchange takes place over the sector boundary as discussed above, and the fact that these are measured ratios instead of experimentally determined); four for every direct sector boundary with the *a*-axis and an additional c^+–c^- apparent *D* (Fig. 1). These five intersector *D* values each provide independent *T* estimates that can be compared against each other for internal consistency. These *D* values can supplement each other for sections that are not preserved or do not develop in some of the sectors, either by the presence of inclusions or stalled growth at some stage of its evolution. Furthermore, because the actual boundary between sectors can be observed, equivalent growth points can be more accurately matched between sectors than is possible for interpolar thermometry. This is especially useful because the c^+ and c^- directions commonly show different and variable growth rates. Most importantly, however, is that re-equilibration is not an issue in intersector thermometry, because diffusion rates are very slow (Voll 1969; von Goerne et al. 1999a). The preservation of sector zoning attests to this slow diffusion and lack of re-equilibration. Any re-equilibration would result in smoothing of the sector boundaries and

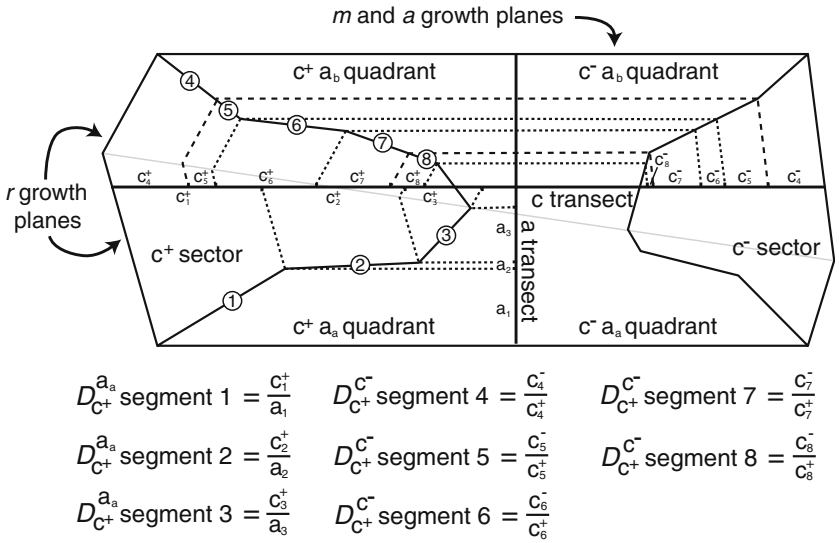

Fig. 1 Schematic drawing of a sector-zoned tourmaline crystal showing the calculation procedure used to derive intersector apparent D values. In this figure, the analysis transects divide the tourmaline into four quadrants, cutting through the sectors. Each sector consists of different segments, defined as sections with equal angle between adjacent sectors. Differences in composition between sectors at the sector boundary are translated parallel to the respective growth surface to the analysis transects. For the c^+–a_a quadrant, the transect is split into three segments with the composition of segment a_1 corresponding to that of c^+_1. D values are derived by dividing the composition of segment c^+_1 by that of a_1. When more analyses are present within a segment, equivalent intermediate positions are calculated by interpolation. To calculate $D^{c^-}_{c^+}$ the c^+ and c^- sectors are linked though their joined a sector. Each kink in the sector boundary angle is translated to the other c-sector, resulting in a total of five segments in this example, where D values are derived by dividing the composition of the c^- segment by its c^+ equivalent

ultimately the disappearance of the sectors, both of which are immediately obvious in back-scattered electron or X-ray imaging.

In this study, we will explore the potential of tourmaline intersector element partitioning as a geothermometer and present preliminary calibrations for thermometers based on c^+–a, and c^+–c^- partitioning of Ti and Ca.

Methods

Tourmalines from four different localities have been used in this study; the Desges river valley in the French Massif Central (MC samples), the Tauern Window in the Alps (KW sample), the island of Syros in the Cyclades (SY sample) and the Berkshire anticlinorium of Western Massachusetts (MA sample). These areas span a range of geotectonic setting, host bulk-rock composition and P–T evolution, as detailed in Table 1. Tourmalines were studied in various crystallographic orientations in both thin-sections and crystal mounts. WDS element mapping was performed on a Cameca SX-100 microprobe at the Department of Earth Sciences, University of Bristol, UK (UoB) using a beam current of 150 nA, 20 kV acceleration voltage and focused beam. Chemical analyses of tourmaline were performed on both the Cameca SX-100 probe and a Jeol-8600 probe at the UoB and the Faculty of Earth Sciences, Utrecht University, The Netherlands. Operating conditions were 20 nA at 20 kV, using a focused beam, and the following standards; wollastonite (Ca), olivine (Si, Mg, Fe), albite (Na, Al), ilmenite (Ti, Mn), orthoclase (K), and MgF_2 (F). A ZAF correction, taking a fixed concentration of B_2O_3 (10.5 wt%) and H_2O (2.5 wt%) into account, was applied to all analyses. The 1 sigma count statistical relative error on the tourmaline analyses is SiO_2 0.5%, Al_2O_3 0.6%, TiO_2 1.3%, FeO 1.7%, MgO 1.3%, CaO 3.2%, Na_2O 5.3%, F 1.5%, and for the trace elements K and Mn, 32 and 38%, respectively. Detection limits are Si 360 ppm, Al 400 ppm, Ti 110 ppm, Fe 370 ppm, Mg 360 ppm, Ca 130 ppm, Na 470 ppm, F 1080 ppm, K 70 ppm and Mn 110 ppm. Alkalis were measured during the first spectrometer run to reduce loss of these elements.

Intersector apparent D values are calculated by matching points in ransects along and perpendicular to tourmaline's c-axis (Fig. 1). This procedure was used, because sector boundaries could not be observed in electron backscatter imaging, but only in element mapping, prohibiting the direct positioning of analysis spots in the same growth zone on either side of this boundary. Element maps formed the base map for matching positions, and secondary electron images of

Table 1 Overview of samples used in this study

Sample	Origin	Rock type	peak P and T
MCVH30	Desges tectonic window, Massif Central, France	Staur–garn–sill meta-pelitic schist	7 kbar, 650°C
MCEOP007	Desges tectonic window, Massif Central, France	kya-garn-plag meta impure sandstone	>7 kbar, 650°C
MCEOP008	Desges tectonic window, Massif Central, France	staur-garn-sill meta-pelitic schist	7 kbar, 650°C
MC32.1	Desges tectonic window, Massif Central, France	staur-garn-sill meta-pelitic schist	7 kbar, 650°C
MC20.4	Desges tectonic window, Massif Central, France	river sediment	–
MA11a	Berkshire anticlinorium, Western Massachusetts, US	garn-staur-biot-paragonite meta-pelite	<6 kbar, 565°C
SY4	Kini Peninsula, Syros, Cyclades, Greece	glauc-omph meta-gabbro	15 kbar, 500°C
KW3a	Lower Schieferhülle, Tauern window, Austria	mafic chlorite-schist	6–8 kbar, 520–600°C

grains after analysis showed the exact position of analysis spots along the transects. Because the sector boundary is irregular in most crystals, transects were divided into sections with a constant angle between sectors as observed in the element maps. Equivalent positions on both *a*- and *c*-transects were then calculated by normalising the *a*-transect part to its *c*-transect equivalent for each section (or vice versa), and compositions for these normalised point positions calculated from the compositions of their nearest neighbours (see supplementary spreadsheet). For complete crystals displaying all sectors this results in four intersector D values for each growth zone. Averages of $D^{a}_{c^+}$ and $D^{a}_{c^-}$ were calculated by averaging over the normalised position along their common *c*-axes, while a $D^{c^-}_{c^+}$ was calculated by correlating the c^+ and c^- sectors along their shared *a*-axes (Fig. 1). A worked example of this procedure for a Massif Central tourmaline grain (sample VH30-3) is provided in the supplementary spreadsheet file.

Core-rim intersector element partitioning profiles

The calculated apparent intersector D values illustrate the element preferences of the different sectors well (Fig. 2). Fractionation is most pronounced for Ca and Ti with the strongest sector differences between the c^+ and c^- sectors. Sector fractionation can however also be observed for Al, and to a lesser extent Fe, but Si is invariably non-sector zoned within analytical and calculation precision. Overall, the c^- sector favours Ca, Ti, Fe, Mg and Na; whereas the c^+ sector favours Al and vacancies on the *X*-site. The *a* sector has an intermediate, but not average, composition between that of the respective *c* sectors. It is also apparent from Fig. 2 that $D^{c^-}_{c^+}$ is mainly controlled by differences in the c^+ sector. Trends in the c^- sector are less well defined and show more scatter. Similar behaviour was found for all tourmalines studied here and the actual contribution of the c^- sector to $D^{c^-}_{c^+}$ diminishes to less than 10% for some crystals. Sperlich (1990) found a similar dominance of changing c^+ composition on the trend in polar $D^{c^-}_{c^+}$ for overgrowths with varying metamorphic grade.

Core to rim profiles for the Massif Central samples show a gradual, systematic convergence to $D = 1$, indicating that fractionation becomes less pronounced from core to rim (Fig. 2). As shown in the introduction of this work, this trend corresponds to an increase in metamorphic temperature and indicates that tourmaline growth is prograde in these samples. However, most tourmaline grains show a reversal of this trend at the outermost rim, with apparent D values diverging from 1. This rim zone is commonly too thin to incorporate accurately in the intersector D calculations and only represents the final data point in Fig. 2. Nonetheless, this reversal can also be recognized in a change from increasing to decreasing X_{Mg} and has been interpreted as the transition from prograde to retrograde growth (van Hinsberg et al. 2006; Bebout and Nakamura 2003). Tourmaline growth thus appears to have taken place during prograde, peak and at the early stages of retrograde conditions and no resorption events can further be recognised.

The Tauern Window sample also shows a decreasing difference between sectors, but the range of values is not as large as that observed for the Massif Central samples. Again, tourmaline growth appears to be prograde, and the limited range in D values probably results from a lower peak-metamorphic temperature for this sample (520–600°C compared to 650°C, Table 1). The Syros sample shows an almost flat pattern, indicating that growth took place over a limited range of conditions (i.e. either fast growth or a stable environment). Interestingly, the absolute contents of Ti and Ca do show variation from core to rim, which suggests that, although the P–T conditions were more or less constant, the chemical environment did change. The Massachusetts sample shows both prograde and retrograde growth and during retrograde growth the apparent D's return to almost starting prograde values. All graphs show scatter around the core to rim trend. Although this can be real, it more likely results from inaccuracies in matching points from different tran-

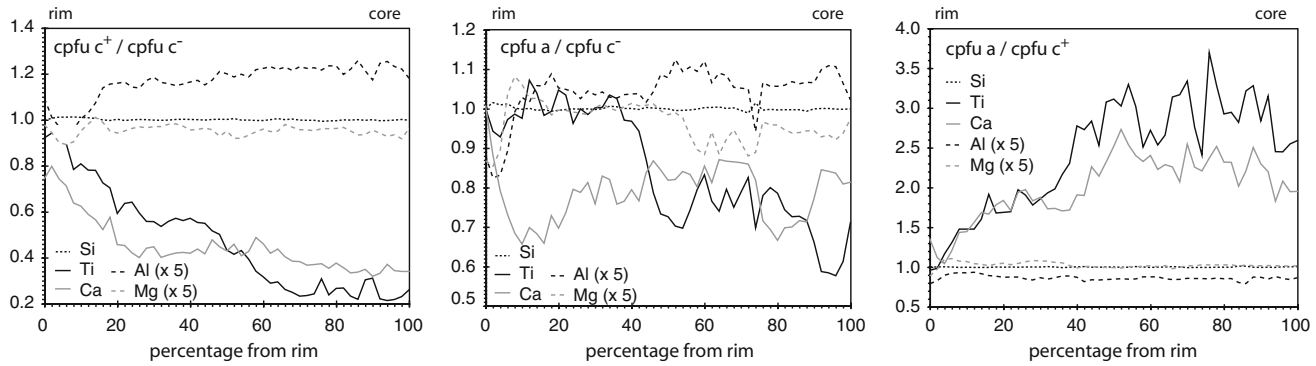

Fig. 2 Core to rim profiles of apparent intersector element partitioning among the c^+–a, c^-–a and c^+–c^- sectors in sample VH30 (shown as apparent D values). Sector fractionation is most pronounced between the c^+ and c^- sectors and for the elements Ca and Ti, which are both enriched in the c^- sector. Al shows opposite behaviour from Ca and Ti. Values converge to one from core to rim, indicating that the intensity of sector zoning decreased during growth for this grain

sects as well as the uncertainty on the analyses. Still, overall trends are consistent.

Calibrating the intersector element partitioning

As previously noted, the convergence in intersector element partitioning has been associated with increasing grade, especially temperature. The core to rim profiles of Massif Central tourmalines further show that these grains preserve a record of conditions from prograde to peak and then to retrograde metamorphism. In order to quantify this record, the intersector partitioning must be calibrated. Because the peak metamorphic conditions are independently known for the Massif Central samples (i.e. 650°C at 7 kbar, van Hinsberg et al. 2007), these conditions can be used as a first calibration point in core-rim profiles that show a reversal from prograde to retrograde growth (samples that lack this reversal can not be guaranteed to have reached peak metamorphism). This gives an apparent D value of 1 for 650°C, which is then also the temperature at which sector zoning disappears.

Additional calibration points to constrain the temperature dependence of intersector partitioning are available from interpolar apparent element partitioning, if one accepts that these are two manifestations of the same process, as suggested here and by Henry et al. (1999). This assumption appears reasonable, because both phenomena result from the same crystallographically controlled process, acting on the same growth surfaces, and, hence, should be affected similarly by changes in P and T. Although there is a large spread in the calibration data (Fig. 3), and the number of data points is limited, there is a consistent trend with temperature. This trend will further be asymptotic in shape towards unity, because there will be no preferential partitioning of elements at high temperature. For polar overgrowths, this convergence is reached at staurolite-zone conditions (i.e. 600–650°C Henry and Dutrow 1996), in good agreement with the observations for intersector partitioning as given above. Combined, this leads us to the eye-ball fit shown in Fig. 3. Obviously, more, and better temperature constrained data points are desirable to improve this fit and we therefore refrain from giving a mathematical expression for this fit. Potential sources of additional calibration points are from P–T estimates for inclusion assemblages, fluid-inclusion thermometry, and the temperature calibrated $\delta^{18}O$ fractionation between tourmaline and quartz (Kotzer et al. 1993).

The resultant T–D calibration between c^+ and c^- polar overgrowths is equivalent to the calibration for c^+ and c^- intersector partitioning. However, for hourglass sector-zoning further intersector partitioning is present between the c^+–a and c^-–a sectors. In fact, it is generally difficult to obtain complete tourmaline crystals cut perfectly parallel to the c-axis and through the centre of the crystal, and c–a partitioning is thus a more practical thermometer. Both the c^+–a and c^-–a apparent D values can be calibrated against c^+–c^- temperatures by matching positions along the c^+–c^- profile to points on the equivalent c–a transects. In other words, by working back from the calculation of c^+–c^- D values (Fig. 1). The resulting calibration graphs (Fig. 4) based on three complete tourmaline grains from the Massif Central show a smooth trend for $D^a_{c^+}$ versus T, converging to 1 at 650°C for both Ca and Ti (Fig. 4a). The trend for $D^a_{c^-}$ versus T is not as well defined and appears to converge to 1 around 550°C for Ti; whereas Ca still shows sector fractionation at 650°C (Fig. 4b). Part of the scatter in Ca for sample MC-VH30 could be due

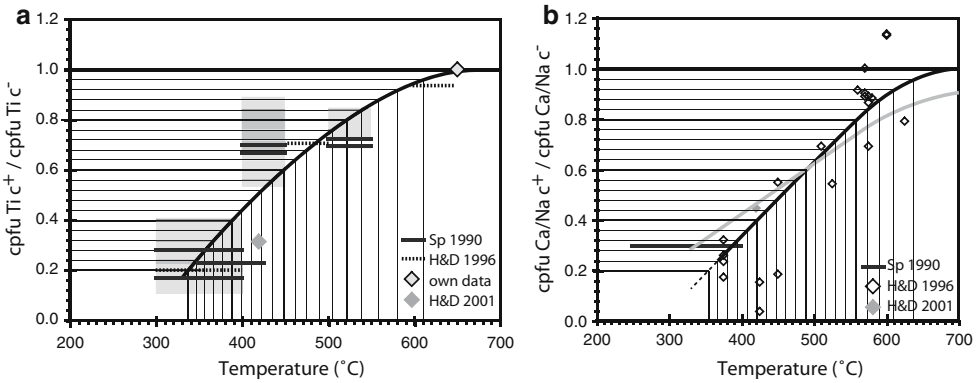

Fig. 3 Calibration diagram and eye-ball best fit curves for Ti and Ca fractionation between the c^+ and c^- sectors. Calibration data are based on interpolar element fractionation in tourmaline and are from Sperlich (1990) and Henry and Dutrow (1996, 2001). The total range in data from Sperlich (1990) is shown by the *grey boxes*, surrounding the median *D* value. A peak metamorphic *D* value of 1 at 650°C provides a further constraint from this work. A shift to the *grey* fit curve in **b** would be required to improve agreement between Ca and Ti derived temperatures

to a crack, which appears to have disturbed Ca concentrations around it. However, c^-–*a* element partitioning does not show well defined trends in any of the samples and c^- sectors are commonly not very regular, especially compared against their c^+ and *a* equivalents. Because the preference mechanism is clearly in place for the c^- sector and is capable of generating substantial element fractionation as observed for c^+ versus *a*, this behaviour of the c^- sector is worrying.

The patchy appearance in Ca and Ti content in a number of c^- sectors suggests that the local, small-scale availability of these elements for incorporation into the tourmaline structure varied. This texture was also observed by van Hinsberg et al. (2006) and attributed to growth exceeding diffusional transport of these elements in the tourmaline growth environment. Henry and Dutrow (1990) observed a similar chemical heterogeneity in tourmaline related to pre-existing host mineralogy and it has also been observed in garnet (Carlson 2002). This small-scale heterogeneity indicates that over- and under-saturation in Ca and Ti may be present for the c^- sector, and further that the saturation level may have varied during growth. Such a local control on element availability would result in a weaker trend for *D* versus *T*, because it will interfere with the temperature dependence, as well as introduce scatter with varying saturation level. Effects for Ca and Ti will further vary independently because local availability (controlled by mineralogy and fluid in the reaction volume) and mobility (controlled by *P, T*, presence and composition of fluid) will change independently for Ca and Ti during progressive growth. This deviation from sector saturation (note that for sector saturation actual saturation of the element in the host rock is not required) will be a function of the actual availability of the element in the environment, but also of growth rate and diffusion velocities, because a slower growth rate at higher diffusion rates should promote sector saturation. Because growth of the *a*-sector is slower than that of the *c*-sectors, sector saturation (or a closer approximation to) can thus be achieved, whereas the c^+ sector does not suffer this complication because it rejects Ca and Ti.

If the c^- sector has a variable saturation level for Ca and Ti, this would limit the use of intersector apparent element partitioning as a thermometer. This effect can further be expected for the interpolar element partitioning data used as calibration points, although it cannot be checked for lack of an equivalent *a*-sector. Because the proximity to saturation appears to vary randomly from core to rim, and the actual saturation concentrations are unknown, no correction can be applied to account for this effect. However, as discussed above, the contribution of the c^- sector to c^+–c^- element partitioning is relatively minor, and generally below 20%. This observation in itself is probably due to the lack of sector saturation, but it also limits the impact of these saturation issues on the intersector and interpolar thermometers. Nonetheless, with the current data, saturation effects on calculated temperatures cannot be sufficiently assessed, and independent calibration points for c^+–*a* partitioning especially, are thus highly desired.

Ca versus Ti derived temperatures

The calibration suite used here, allows us to independently derive temperatures from Ca and Ti apparent partitioning, respectively, (other elements such as Na

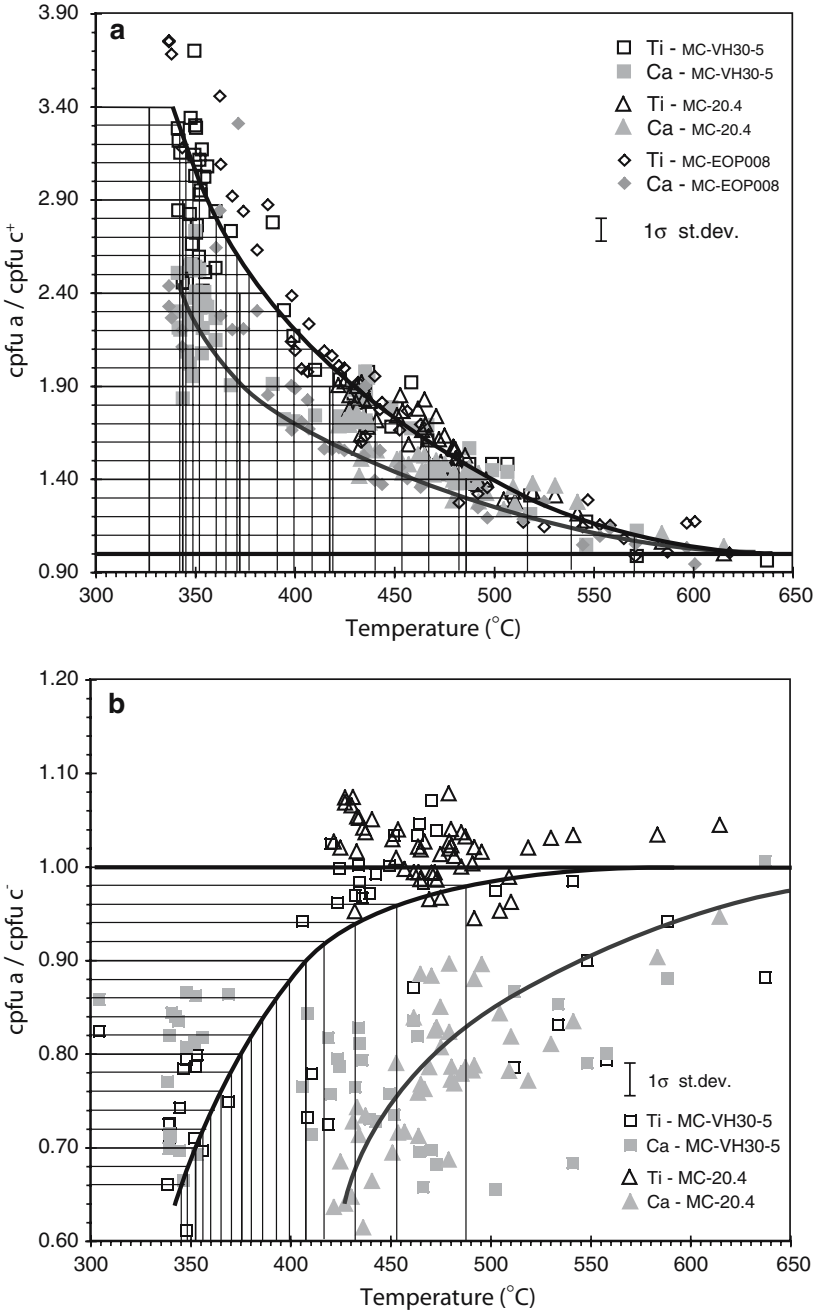

Fig. 4 Calibration diagrams and eye-ball fit curves for Ca and Ti fractionation between the *c* and *a* sectors, as calculated from c^+ to c^- temperatures for three complete tourmaline crystals. Fractionation trends with temperature are well defined for c^+ versus *a*, but show significant scatter for its c^- versus *a* equivalent. Overall, fractionation decreases asymptotically to one with increasing temperature. The typical propagated 1 sigma standard deviation on the calculated *D* values is also shown. Its resultant uncertainty in temperature varies from circa 100°C at 650°C to 10°C at 350°C for the c^+–*a* curves and 100°C at 500°C to 20°C at 350°C for the c^-–*a* data

or Al could be used as well, but given that partitioning is most pronounced for Ca and Ti, these elements have the smallest associated uncertainty). In core-to-rim profiles, Ca and Ti temperatures display the same trends and both display the observed reversal from prograde to retrograde conditions in the rim of Massif Central and Massachusetts samples. Plotted against each other the temperatures show a strong correlation (Fig. 5). However, Ca derived temperatures define a somewhat shallower trend than Ti derived equivalents. For the high temperature section of the profile it is more difficult to match points between sectors because the thickness of growth zones decreases, which can explain part of the observed discrepancy. Especially, because this section contains a distinct Ca-spike, on the scale of individual microprobe spots.

The agreement between Ca and Ti derived temperatures can be improved by making the calibration curve for Ti in Fig. 3 steeper or that of Ca shallower. A steeper fit through the Ti data is difficult to accommodate, but a shallower fit through the Ca data is possible and would in fact be in better agreement with

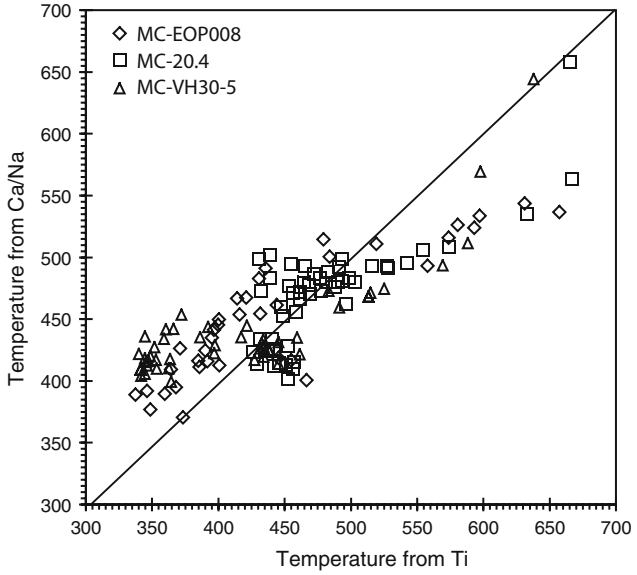

Fig. 5 Ca versus Ti derived temperatures based on c^+–c^- intersector thermometry show a good correlation, but deviate from the 1:1 line. This disagreement is probably mainly related to uncertainties in the calibration data, especially for Ca partitioning. A shift to the *grey* fit in Fig. 3b would result in consistent Ca and Ti derived temperatures

data from Sperlich (1990). The modified fit (grey curve in Fig. 3b) is still in reasonable agreement with most calibration data. However, it does not represent the best fit through the data, showing that more calibration data are needed to validate the modified fit. Convergence of the *c*-sector compositions is slower in the new fit, with *D* values less than 1 even at 700°C. Such a difference in convergence rate between Ca and Ti is probably real and related to differences in the preference mechanism controlling Ti and Ca incorporation on the growth surface. Ti is controlled by polar surface charge, but Ca is in part also controlled by differences in *X*-site exposure on the growth surfaces in the c^+ and c^- growth directions (van Hinsberg et al. 2006). Although the partitioning capacity of both mechanisms can be expected to decrease with increasing temperature, this will happen at different rates, and site morphology control will probably have a more persistent character.

Temperature profiles for tourmaline

Using the thermometers established above, the element partitioning profiles between the sectors can be converted to *T* profiles (Fig. 6). These indicate that tourmaline records growth at a wide range of conditions. The Massif Central samples record first appearance of tourmaline at circa 350°C followed by continuous growth at increasing temperature up to the peak conditions at 650°C. It is also apparent that growth rates varied from core to rim, with most growth confined to the initial appearance of tourmaline. Growth further took place in steps, especially at low temperature, suggesting that it is mainly controlled by the breakdown of phases releasing B into the host rock as *T* increases (c.f. Henry and Dutrow 1996). Peak metamorphic tourmaline growth is limited in all samples and is followed by retrograde growth that records temperatures down to circa 450°C in several samples. This same retrograde growth is present in most grains, but commonly produces thin rims that are too small to incorporate in the apparent *D* calculations as discussed above.

The tourmaline grain from Massif Central sample EOP007 (Fig. 6e) is an interesting sample because it formed in a metapsammite, rather than the pelitic composition of the other Massif Central samples. It also shows evidence for higher-pressure peak metamorphic conditions, because it contains kyanite instead of sillimanite in the peak metamorphic assemblage. Despite these differences this tourmaline shows a similar trend in temperature, albeit starting at higher *T*, and records the same peak metamorphic temperature. This suggests that the intersector thermometer has little pressure, or bulk rock compositional dependence.

Massachusetts sample MA11a (Fig. 6f) records a similar history as the Massif Central samples. The first appearance of tourmaline is at circa 400°C and is followed by little growth at increasing temperatures up to a peak of 565°C. It further preserves retrograde growth at conditions down to 400°C. The break from prograde to retrograde conditions in this tourmaline is marked by a distinct growth band rich in Ti (Fig. 6c) and is further characterized by a change from Al ''undersaturated'' (i.e. $Al^Z + Al^Y < 6$) to ''saturated'' tourmaline. The peak metamorphic temperature for this sample as determined from Ti in biotite thermometry (Henry et al. 2005) is 565 ± 11°C, showing remarkable agreement. This agreement further indicates that the technique gives meaningful results.

The Tauern Window tourmaline sample records first growth at 350°C, followed by a second episode of tourmaline growth between 400 and 450°C (Fig. 6g). These temperatures are similar to those observed for growth bursts in the Massif Central samples, and suggests that tourmaline growth is related to the same mineral reactions in both areas, independent of their different host bulk rock composition (assuming similar pressures). The 450°C peak temperature recorded by the Tauern Window sample is lower than the peak

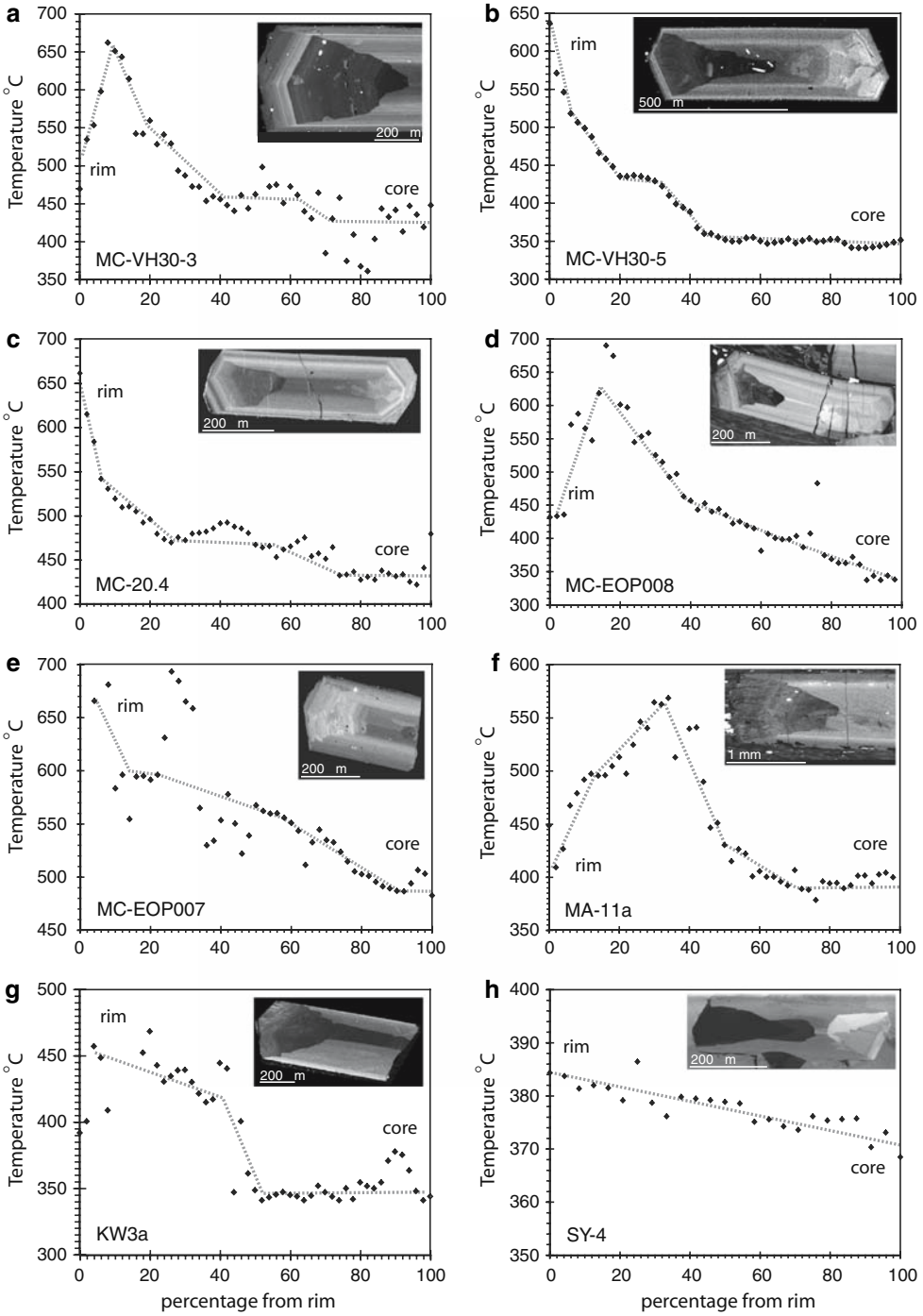

Fig. 6 Temperature profiles for a selection of crystals from the French Massif Central (*MC*), the Tauern Window in the Alps (*KW*), the island of Syros in the Cyclades,Greece (*SY*) and the Berkshire anticlinorium in western Massachusetts (*MA*). All crystals show an increase in temperature from core to rim, suggesting that they formed during the prograde history of their respective host rocks. Several of the MC samples, as well as the Massachusetts sample also record growth during the retrograde evolution. Growth is step-like in nature and first appearance of individual tourmaline crystals occurs at different points on the overall temperature history. The insets show WDS element maps of the analysed crystals with their respective (sector) zoning. All profiles are from rim to core, with temperatures from individual sector boundaries averaged. For complete crystals (**b**, **c**, **d**, **h**) the c^+–c^- partitioning has been included in the average as well. Sample MC-VH30-5 is our main calibration sample and therefore shows little scatter in the temperature profile

metamorphic temperature for this area. This might indicate that growth of tourmaline stalled at 450°C. However, the metamorphic history of this area is complicated with both Hercynian and Alpine metamorphic imprints being present (G. Franz, personal communication), and it is thus clear that tourmaline has only recorded growth during part of this history.

The Syros sample shows little variation in temperature, although there is a gradual increase from 370 to 385°C from core to rim (Fig. 6h). This temperature difference is too small to conclusively assign it to growth during the prograde evolution of the area. However, tourmaline's intimate intergrowth relations with fresh omphacite, garnet and epidote suggest that it did indeed grow during prograde conditions.

Comparison of the different Massif Central samples shows that they record different parts of the overall history. Especially the nucleation of individual tour-

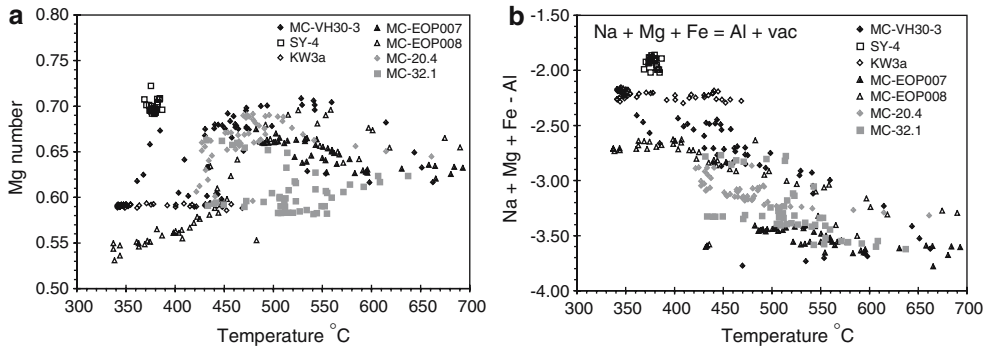

Fig. 7 Composition of the *a*-sector for a number of tourmaline crystals versus the temperature derived from intersector thermometry. There is no strong overall trend in X_{Mg} versus T (**a**), although individual grains do commonly show a systematic behaviour, suggesting that X_{Mg} is mainly controlled by host rock composition and mineral paragenesis. Na and Al do show a strong correlation with T, which is even more pronounced when expressed in terms of the dominant exchange vector in these tourmalines (**b**)

maline grains varies, ranging from 350 to 500°C, with higher temperatures found for more psammitic host-rock compositions. Because tourmaline growth is mainly controlled by the availability of B in the host rock, this stacked appearance is probably related to an inhomogeneous distribution of B, B-containing phases in the protolith or incursion of B-bearing fluids. Rapid growth of tourmaline can further deplete the rock of available B, thus stalling the nucleation of new grains until a new B-releasing reaction takes place. However, all grains do record peak metamorphic growth, thus allowing different profiles to be matched. When this is done for temperature, distinct marker bands in the tourmaline crystals (e.g. growth zones rich in Ca Fig. 6) line up as well, showing that temperatures are consistent among crystals and that individual grains record the same chemical events in the host environment. Signatures are further not destroyed or even disturbed when crystals pass into the sedimentary record (e.g. MC-20.4).

Identifying the reactions responsible for tourmaline growth stages is difficult, because the *P*–*T* positions of prograde reactions at low grade are not well constrained. The initial appearance of tourmaline in both Tauern Window and Massif Central samples at circa 350°C is probably related to the breakdown of clay minerals to form white mica (Henry and Dutrow 1996). However, allowing for the uncertainty on this temperature, it might also be related to the breakdown of pyrophyllite to form andalusite or kyanite (depending on *P*). The growth stage at 450°C could be related to the appearance of biotite in these rocks, either from the breakdown of chlorite + detrital K-feldspar or from chlorite + muscovite (Spear 1993). A distinct growth band, rich in Ca, at about 550°C fits well with the chlorite + garnet to staurolite + biotite reaction, when calculated for these bulk rock compositions (van Hinsberg et al. 2007), with Ca derived from the breakdown of garnet. The "Al-under-saturated" character of the Massachusetts tourmaline further suggests that its host had not reached the sillimanite isograd during prograde metamorphism and was hence not saturated in Al-silicate, in agreement with its peak metamorphic temperature and petrography. Trace elements in these growth zones can be expected to provide a better signature of reactions responsible for tourmaline growth and when combined with the *T* information from intersector partitioning could prove to become a valuable tool to constrain metamorphic reactions in *P*–*T* space.

T–*X* profiles

Temperatures from intersector element partitioning also allow the effects of temperature on tourmaline composition to be assessed. To avoid interference on these compositions from strong c^+–c^- sector zoning effects, the *a*-sector composition is used, because it appears to represent the composition of tourmaline that is not sector zoned (van Hinsberg et al. 2006). Plotting composition against temperature shows that there is no significant trend in either Ca or Ti content with temperature for the samples studied here. This indicates that absolute concentrations do not affect intersector partitioning, in agreement with the observations for sample SY-4 as discussed above. This is an important finding supporting the overall technique, but it also suggests that the effects of lack of saturation in the c^- sector are minor. X_{Mg} does not show a well-defined overall trend with temperature, especially if the Syros sample is taken into account (Fig. 7a).

However, individual samples (e.g. MC-EOP008) commonly show clear trends. This is probably due to the initial value of X_{Mg} being controlled by host rock composition; whereas the variation in X_{Mg} reflects the evolution of the mineral paragenesis of the rock. Na and Al, on the other hand, both show a strong overall correlation with temperature; Al increases with temperature and Na decreases. Von Goerne et al. (1999b) noted a similar inverse relation between these elements with varying temperature in their experiments. This inverse correlation between Na and Al is consistent with the main exchange vector in these tourmalines, which is $Na^X + Mg^Y + Fe^Y$ for vacancy$^X + Al^Y$ (van Hinsberg et al. 2006). In fact, when this relation is plotted against temperature (Fig. 7b) there is an even stronger correlation, suggesting that this exchange is strongly temperature controlled. The consistency of this trend over the wide range of temperatures, bulk rock compositions and mineral parageneses is further interesting, because it indicates that this temperature dependence cannot be the result of simple exchange with a mineral or mineral assemblage as none span the range in these conditions. Rather, it appears to be a property of tourmaline itself or related to exchange with a fluid. If this observation and its controlling mechanism are correct, this is another potential thermometer.

Conclusions

Intersector element partitioning in hourglass sector zoned tourmaline shows a strong temperature dependence, which can be used as a geothermometer, applicable to a wide range of temperatures (at least 350 to 650°C) and bulk rock compositions. It appears to show little, if any, pressure dependence. The examples discussed here, show that it is especially powerful in providing information on the prograde evolution of its host rock, where T information from other sources is commonly scarce. The uncertainty in the empirical calibration fit is the only caveat to limit its widespread application. More calibration points would help to refine the curves in Figs. 3 and 4 and calibration sources other than interpolar partitioning are particularly desired, because of the potential for over or under-saturation in Ca and Ti in the c^- sector. This latter issue should also be studied in more detail to determine whether it is real and if it affects the calculated temperatures. Carbonate-bearing pelites should provide the ideal host rock for such a study. Nevertheless, both Ca and Ti intersector element partitioning as applied here are valuable tools to constrain the temperature history of tourmaline crystals and their host environments. Combining these temperatures with tourmaline composition and trace element variations can further provide insight into the element mobility with changing metamorphic grade. Finally, temperature and compositional records are preserved in detrital grains and these may thus provide tantalising insight into the nature and evolution of their eroded hosts.

Acknowledgments We thank Stuart Kearns for advice and help with all aspects of microbeam analyses, and for countless discussions. Simon Vriend is thanked for arranging access to the Utrecht University EMP facilities in 2002. VvH acknowledges financial support from the University of Bristol through a strategic postgraduate scholarship. Part of this research was funded through a NERC small research grant.

References

Bebout GE, Nakamura E (2003) Record in metamorphic tourmalines of subduction-zone devolatilization and boron cycling. Geology 31:407–410

Blencoe JG, Guidotti CV, Sassi FP (1994) The paragonite–muscovite solvus: II numerical geothermometers for natural quasibinary paragonite–muscovite pairs, Geochim Cosmochim Acta 58:2277–2288

Bohlen SR, Wall VJ, Boettcher AL (1983) Experimental investigations and geological applications of equilibria in the system $FeO–TiO_2–Al_2O_3–SiO_2–H_2O$. Am Mineral 68:1049–1058

Carlson WD (2002) Presidential address; scales of equilibrium and rates of equilibration during metamorphism. Am Mineral 87:185–204

Elkins LT, Grove TL (1990) Ternary feldspar experiments and thermodynamic models. Am Mineral 75:544–559

Faure G (1986) Principles of isotope geology, 2nd edn. Wiley, London, 589pp

von Goerne G, Franz G, Wirth R (1999a) Hydrothermal synthesis of large dravite crystals by the chamber method. Eur J Mineral 11:1061–1078

von Goerne G, Franz G, Robert JL (1999b) Upper thermal stability of tourmaline + quartz in the system $MgO–Al_2O_3–SiO_2–B_2O_3–H_2O$ and $Na_2O–MgO–Al_2O_3–SiO_2–B_2O_3–H_2O–HCl$ in hydrothermal solutions and siliceous melts. Can Mineral 37:1025–1039

Grew ES, Anovitz LM (1996) Boron: mineralogy, petrology, and geochemistry, Rev Mineral 33, Mineralogical Society of America, Washington, 864pp

Grover JE, Orville PM (1969) The partitioning of cations between coexisting single- and multi-site phases with application to the assemblages: orthopyroxene–clinopyroxene and orthopyroxene–olivine. Geochim Cosmochim Acta 33:205–226

Henry DJ, Dutrow BL (1990) Ca substitution in Li-poor aluminous tourmaline. Can Mineral 28:111–124

Henry DJ, Dutrow BL (1992) Tourmaline in a low-grade clastic metasedimentary rock: an example of the petrogenetic potential of tourmaline. Contrib Mineral Petrol 112:203–218

Henry DJ, Dutrow BL (1996) Metamorphic tourmaline and its petrologic applications. In: Grew ES, Anovitz LM (eds) Boron: mineralogy, petrology, and geochemistry. Rev Mineral 33:503–557

Henry DJ, Dutrow BL (2001) Compositional zoning and element partitioning in nickeloan tourmaline from a metamorphosed karstbauxite from Samos, Greece. Am Mineral 80:1130–1142

Henry DJ, Kirkland BL, Kirkland DW (1999) Sector-zoned tourmaline from the cap rock of a salt dome. Eur J Mineral 11:263–280

Henry DJ, Guidotti CV, Thomson JA (2005) The Ti-saturation surface for low-to-medium pressure metapelitic biotite: implications for geothermometry and Ti-substitution mechanisms. Am Mineral 90:316–328

van Hinsberg VJ, Schumacher JC, Kearns S (2004) A new type of sector zoning in tourmaline: Inferences and applications. Geol Soc Am Abstr Prog 36:225

van Hinsberg VJ, Schumacher JC, Kearns S, Mason PRD, Franz G (2006) Hourglass sector zoning in metamorphic tourmaline and resultant major and trace element fractionation. Am Mineral 91:717–728

van Hinsberg VJ, Zinngrebe E, de Wijs CJ, Vriend SP (2007) Thermo-chronology of the Barlet metamorphic basement unit: evidence for a Stephanian thermal event linked to Sb mineralizations in the Haut Allier, France, (in press)

Holdaway MJ (2000) Application of new experimental and garnet Margules data to the garnet–biotite geothermometer. Am Mineral 85:881–892

Holdaway MJ (2001) Recalibration of the GASP geobarometer in light of recent garnet and plagioclase activity models and versions of the garnet–biotite geothermometer. Am Mineral 86:1117–1129

Kotzer TG, Kyser TK, King RW, Kerrich R (1993) An empirical oxygen- and hydrogenisotope geothermometer for quartz–tourmaline and tourmaline–water. Geochim Cosmochim Acta 57:3421–3426

Pownceby MI, Wall VI, O'Neill HS (1991) An experimental study of the effect of Ca upon garnet–ilmenite Fe–Mn exchange equilibria, Am Mineral 76:1580–1588

Pyle JM, Spear FS (2000) An empirical garnet (YAG)—xenotime thermometer, Contrib Mineral Petrol 138:51–58

Pyle JM, Spear FS, Rudnick RF, McDonough WF (2001) Monazite–xenotime–garnet equilibrium in metapelites and a new monazite–garnet thermometer, J Petrol 42:2083–2107

Spear FS (1993) Metamorphic phase equilibria and pressure–temperature–time paths. Miner Soc Am Monogr 1:799

Sperlich R (1990) Zoning and crystal chemistry of tourmalines in prograde metamorphic sequences of the Central Alps. PhD thesis, University of Basel, Switzerland, 51pp

Sperlich R, Giere R, Frey M (1996) Evolution of compositional polarity and zoning in tourmaline during prograde metamorphism of sedimentary rocks in the Swiss Central Alps. Am Mineral 81:1222–1236

Voll G (1969) Klastische Mineralien aus den Sedimentserien der Schottischen Highlands und ihr Schiksal bei aufsteigender Regional- und Kontaktmetamorphose. Habilitations These, Technische Universität Berlin

Zack T, Moraes R, Kronz A (2004) Temperature dependence of Zr in rutile: Empirical calibration of a rutile thermometer. Contrib Mineral Petrol 148:471–488